

Article

Optimal Design of Ejector Nozzle Profile with Internal and External Integrated Flow

Yihe He, Xiaojuan Shi * and Honghu Ji

College of Energy and Power Engineering, Nanjing University of Aeronautics and Astronautics, Nanjing 210016, China; hyhnuaa@nuaa.edu.cn (Y.H.); jhhpe@nuaa.edu.cn (H.J.)

* Correspondence: shixiaojuan@nuaa.edu.cn

Abstract: Based on the orthogonal experimental method, a simulation case of the flow field of the ejector nozzle was designed to investigate the influence of the structural parameters of the ejector nozzle on the internal and external flow. This study explored the effects of throat area, outlet area, throat position, and ejector nozzle length on the ejector flow rate ratio, thrust coefficient, and net thrust coefficient. Subsequently, flow path geometry optimization was conducted to maximize the thrust coefficient or net thrust coefficient. The results revealed that the throat area ratio and the outlet area of the ejector nozzle are the primary factors affecting the aerodynamic performance. Compared to the baseline ejector nozzle model, the optimal model for thrust coefficient exhibited a 16.333% improvement, while the optimal model for net thrust coefficient demonstrated a significant enhancement of 46.674%.

Keywords: internal and external integrated flow; ejector nozzle; optimal design; thrust; afterbody drag

1. Introduction

With the continuous development of aircraft, the integration of flight and engine has become a major challenge that cannot be ignored, and a large number of related studies have been conducted [1–5]. As a key component of the engine, the integrated design of the nozzle and the aircraft afterbody has become the core focus of the research on the integration of flight and engine. The interaction between the nozzle exhaust and the external flow will change the pressure distribution at the rear end of the airframe, affect the degree of gas expansion, and interfere with the airflow around the airframe, resulting in increased flight resistance. Research has found that the afterbody resistance of the airframe can account for 38% to 50% of the total resistance of the aircraft [6], of which about one-third is related to the tail nozzle and the afterbody.

Through a simple structure, utilizing high-speed airflow to inject low-speed airflow, there is a wealth of related research and experiments on ejector nozzles in aerospace engineering and energy fields [7–10].

In the field of aviation, by effectively utilizing the overflow of the boundary layer from the inlet, the ejector nozzle can enhance propulsion performance and provide cooling and protection for the nozzle wall, as verified in engineering applications [11]. Additionally, the ejector nozzle plays a role in reducing afterbody drag. There is evidence suggesting that the use of adjustable ejector nozzles can decrease the afterbody angle, thereby reducing afterbody drag [12].

Numerous scholars have conducted a series of studies on the flow field structure of ejector nozzles. In ejector nozzles, the dynamic mixing of fluids is the primary mode of momentum transfer [13,14]. The degree of mixing between these two streams of fluid occurs in the free shear layer [15] and determines the performance of the ejector nozzle.

Levis E. Wallner and others [16,17] investigated the relationships between the suction and thrust characteristics of ejector nozzles and the primary flow pressure ratio, diameter



Citation: He, Y.; Shi, X.; Ji, H. Optimal Design of Ejector Nozzle Profile with Internal and External Integrated Flow. *Aerospace* **2024**, *11*, 184. <https://doi.org/10.3390/aerospace11030184>

Received: 23 December 2023

Revised: 25 January 2024

Accepted: 25 January 2024

Published: 26 February 2024



Copyright: © 2024 by the authors. Licensee MDPI, Basel, Switzerland. This article is an open access article distributed under the terms and conditions of the Creative Commons Attribution (CC BY) license (<https://creativecommons.org/licenses/by/4.0/>).

ratio, and spacing ratio. In the 1950s, NASA conducted extensive experimental research on ejector nozzles [18–20], maintaining a constant primary-to-secondary pressure ratio, to study the relationship between the geometric dimensions of ejector nozzles and their suction and thrust characteristics.

Kumar et al. [21] explored the flow field structure in the vacuum ejector device and further studied the vortex characteristics of the secondary flow backflow through experiments. Karthick et al. [22] carried out a study on the mixing characteristics of the main and secondary flow of a supersonic ejector in a rectangular ejector and used PLMS technology to reveal the structure of the flow field, such as the shock node and mixing layer in the ejector and the instability of the flow. Zohar Hoter [23] optimized a one-sided mixer–ejector nozzle by numerical studies. It was found for ejector gap height and ejector flap leading edge radius, while streamwise throat location had little effect on entrainment. Changjie Ge [24] studied the effects of longitudinal distance between the engine nozzle exit and aircraft surface and radius of the ejector nozzle exit on the performance of the integrated ejector nozzle system. Ma [25] studied internal and external field characteristics of the conformal asymmetric nozzle of a flying wing Unmanned Aerial Vehicle in the typical flight condition. The results show that under a fixed blow-down ratio of the engine nozzle, the main flow field characteristics of the afterbody nozzle can be effectively improved by reasonably optimizing the secondary flow channel and increasing the blow-down ratio of secondary flow. Cai and colleagues [26] conducted a simulation analysis on the impact of the entrainment coefficient on the flow and thrust performance of ejector nozzles, proposing the existence of two typical states, “wall-attached” and “detached”, in the internal shear layer of ejector nozzles. Huang [27,28] and others studied the flow characteristics of ejector nozzles with third-stream assisted air intake.

From the above discussion, research on ejector nozzles has mainly focused on the ejector structure and internal flow characteristics. There are limited explorations into internal and external integrated flow and the impact of the ejector nozzle on the drag of afterbody.

For further application of the ejector nozzle, the ejector nozzles investigated in this study were integrated into the aircraft tail. Using the orthogonal experimental method, cases were designed to explore the impact of ejector nozzle geometry parameters on their aerodynamic performance. Based on these investigations, optimization was carried out with the objectives of maximizing thrust coefficient and net thrust coefficient. The resulting optimal models aim to serve as a reference for the design of ejector nozzles with internal and external integrated flow.

2. Research Object and Key Design Parameters

2.1. Research Object

This study focuses on a symmetrical axisymmetric ejector nozzle integrated with the afterbody of an aircraft. It includes a convergent–divergent ejector sleeve added outside the converging main nozzle. The aircraft afterbody consists of a straight section and a converging section, connected to the exit of the ejector nozzle. Due to the symmetry of the structure about the nozzle axis, a two-dimensional model is employed for the study. Figure 1 provides a schematic diagram of the two-dimensional geometric model. In the ejector nozzle, the primary flow flows out through the convergent main nozzle and mixes with the secondary flow, and then flows out of the ejector nozzle together.

In this study, the aerodynamic performance of the ejector nozzle was investigated under the conditions of an aircraft flying at a Mach number of 1.05. The geometric structure of the main nozzle remained unchanged, and both the total pressure and total temperature of the primary flow and secondary flow were kept constant. For the ejector nozzle, the geometric parameters include the throat radius R_s , outlet radius R_e , axial distance between the throat of the ejector nozzle and the outlet of the main nozzle L_s , and axial distance between the outlet of the ejector nozzle and the outlet of the main nozzle L . The converging

section of the afterbody changes in response to variations in the ejector nozzle, and its curve is described by the following equation:

$$\frac{r}{R_{10}} = 1 - \left(1 - \frac{R_e}{R_{10}}\right) \left(\frac{x}{L}\right)^n \quad (1)$$

where R_{10} is the maximum radius of the afterbody, x is the axial distance from the main nozzle outlet, r is the circumferential distance, and n is selected as 3 with reference to *Aircraft Engine Design* [29].

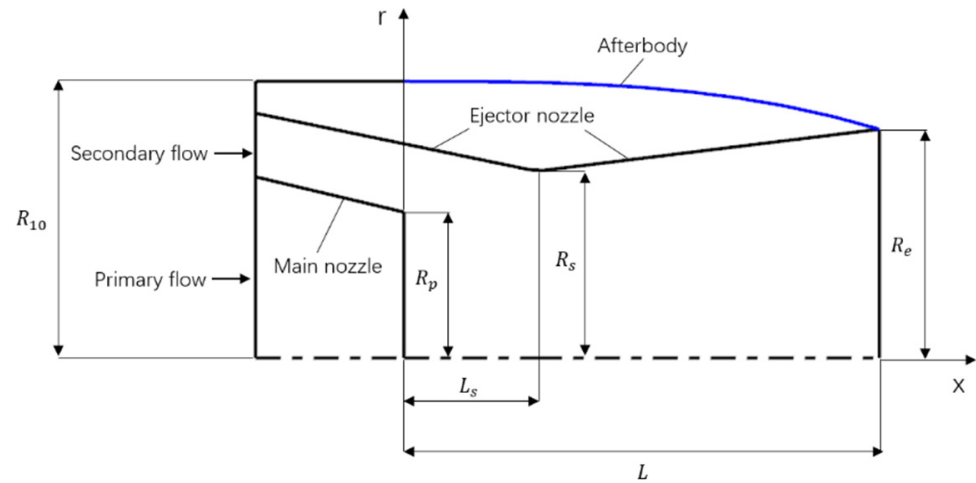


Figure 1. Schematic diagram of the ejector nozzle geometry model.

2.2. Key Design Parameters and Their Variation Range

The design parameters for the ejector sleeve are nondimensionalized using the outlet parameters of the main nozzle. The key design parameters include the ratio of ejector sleeve throat area to main nozzle outlet area A_s/A_p , the ratio of ejector sleeve outlet area to main nozzle outlet area A_e/A_p , the ratio of axial distance between ejector sleeve throat and main nozzle outlet to main nozzle outlet diameter L_s/D_p , and the ratio of axial distance between ejector sleeve outlet and main nozzle outlet to main nozzle outlet diameter L/D_p . The parameter ranges are referenced from the literature [16] and are selected as $1.23 \leq A_s/A_p \leq 1.85$, $1.54 \leq A_e/A_p \leq 2.91$, $0 \leq L_s/D_p \leq 0.45$, and $1.10 \leq L/D_p \leq 1.65$.

3. Optimization Design Method

3.1. Definition of Aerodynamic Performance

The aerodynamic performance of the studied ejector nozzle in this paper is characterized by three parameters: the ejector flow rate ratio, thrust coefficient, and net thrust coefficient.

The ejector flow ratio \dot{m}_s/\dot{m}_p is defined as the ratio of the secondary flow to the primary flow.

The thrust of the ejector nozzle is compared with the ideal thrust of a Laval nozzle under isentropic, fully expanded conditions.

The thrust coefficient C_f is defined as the ratio of the actual thrust generated by the ejector nozzle to the ideal fully expanded thrust of the primary flow:

$$C_f = \frac{F_{ej}}{F_{ip}} \quad (2)$$

According to the primary flow parameters, the ideal fully expanded thrust F_{ip} of the Laval nozzle can be calculated as follows:

$$F_{ip} = \dot{m}_{ip} U_{ip} \quad (3)$$

where \dot{m}_{ip} is the ideal flow rate and U_{ip} is the nozzle outlet velocity during isentropic complete expansion of the gas flow. The expression is as follows:

$$\dot{m}_{ip} = P_t A_8 \frac{k \sqrt{\left(\frac{2}{k+1}\right)^{\frac{k+1}{k-1}}}}{\sqrt{kRT_t}} \quad (4)$$

$$U_{ip} = \sqrt{2 \frac{kRT_t}{k-1} \left[1 - \left(\frac{P_a}{P_t}\right)^{\frac{k-1}{k}}\right]} \quad (5)$$

The actual thrust F_{ej} of the ejector nozzle is calculated based on CFD results:

$$F_{ej} = \dot{m}_{ej} U_x + (P_e - P_a) A_e \quad (6)$$

where \dot{m}_{ej} is the flow rate of the ejector nozzle, A_e , P_e , and U_x are the area, static pressure, and axial velocity of the ejector nozzle outlet, and P_a represents the ambient pressure.

The net thrust coefficient C_{f-net} takes into account the influence of afterbody drag on the thrust of the ejector nozzle and is defined as follows:

$$C_{f-net} = \frac{F_{ej} - D_{aft}}{F_{ip}} \quad (7)$$

where D_{aft} is the afterbody drag.

The afterbody drag includes pressure drag and friction drag, which are the integrals of the pressure difference force and friction force along the axial direction of the nozzle from the cross section of the afterbody of the aircraft to the nozzle outlet cross-section. The calculation formula is as follows:

$$D_{aft} = - \int (P - P_a) dA + X_f \quad (8)$$

where P is the static pressure on the afterbody surface and X_f is the friction drag.

3.2. Mathematical Description of Optimization Design

Design parameters that describe the ejector nozzle profile can be considered as inputs and for each set of inputs, there are corresponding values of \dot{m}_s/\dot{m}_p , C_f , and C_{f-net} , which are the responses of inputs. The ejector nozzle profile optimization is to obtain the maximum C_f or C_{f-net} responses by taking values of the parameters within the variation range.

With the maximization of the thrust coefficient as the optimization objective, the mathematical description of the surface optimization design is as follows:

$$\begin{aligned} \max \quad & C_f = f(A_s/A_p, A_e/A_p, L_s/D_p, L/D_p) \\ \text{s.t.} \quad & 1.23 \leq A_s/A_p \leq 1.85, \\ & 1.54 \leq A_e/A_p \leq 2.91, \\ & 0 \leq L_s/D_p \leq 0.45, \\ & 1.07 \leq L/D_p \leq 1.61 \end{aligned}$$

With the maximization of the net thrust coefficient as the optimization objective, the mathematical description of the surface optimization design is as follows:

$$\begin{aligned} \max \quad & C_{f-net} = f(A_s/A_p, A_e/A_p, L_s/D_p, L/D_p) \\ \text{s.t.} \quad & 1.23 \leq A_s/A_p \leq 1.85, \\ & 1.54 \leq A_e/A_p \leq 2.91, \\ & 0 \leq L_s/D_p \leq 0.45, \\ & 1.07 \leq L/D_p \leq 1.61 \end{aligned}$$

3.3. Optimization Design Process

The optimization process for the ejector nozzle profile is illustrated in Figure 2, with the main steps outlined as follows:

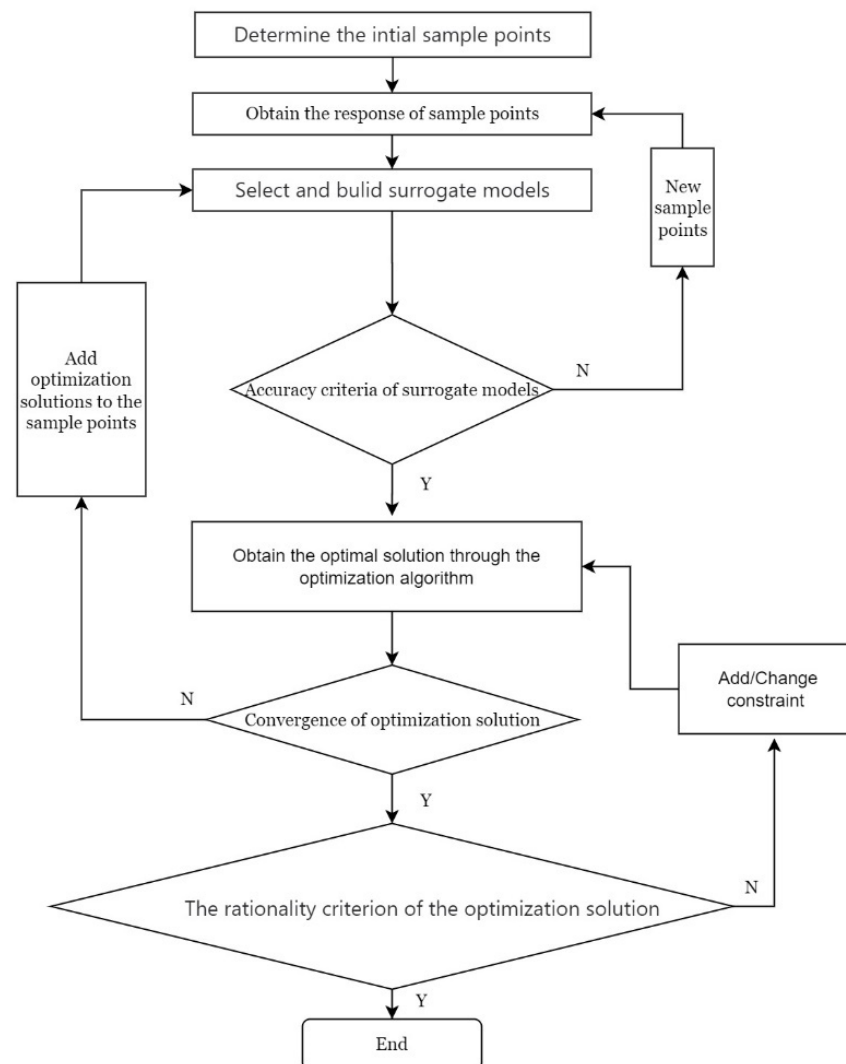


Figure 2. Ejector nozzle optimization design algorithm.

(1) Utilize the orthogonal experimental design method to determine initial sample points systematically. (2) Establish a model and numerically compute the response for each sample point. (3) Based on the initial sample points and their responses, select and construct a surrogate model representing the relationship between aerodynamic parameters and design parameters. (4) Use new responses from external sample points to evaluate the accuracy of the surrogate model, and if the accuracy falls below the required threshold, add the new sample points to the initial sample points and repeat steps 2 to 4. Continue

this process until a surrogate model with satisfactory accuracy is obtained. (5) Utilize the surrogate model and optimization algorithm to obtain the optimal solution under given constraints. (6) Compare simulation results with the predictions of the surrogate model to assess convergence. If convergence is not achieved, add the results to the initial sample points and repeat steps 2 to 6 until the desired convergence is reached. (7) Evaluate the reasonability of the optimization results. If deemed unreasonable, add or modify constraints, and repeat steps 5 to 7 until satisfactory optimization results are obtained.

This study employs the Kriging model as the surrogate model. Initially proposed by Danie Krige, Kriging is an unbiased estimation model that minimizes variance. It features local estimation capabilities, making it particularly effective in achieving desirable fitting results for problems with high nonlinearity [30,31]. In the field of surface design, researchers such as Shi et al. [32–36] have achieved favorable results using the Kriging model.

For the accuracy assessment of the surrogate model, the evaluation metrics include the root mean square error (RMSE) and the max error. Taking the thrust coefficient as an example, they are defined as follows:

Precision testing is conducted by constructing cases with external sample points. The thrust coefficient obtained from computational fluid dynamics (CFD) numerical simulations is denoted as $C_{f,CFD}$, while the thrust coefficient obtained from the surrogate model is denoted as $C_{f,Kriging}$. The expressions for the root mean square error (RMSE) and the max error of the surrogate model are as follows:

$$RMSE = \sqrt{\frac{1}{n} \sum_{i=1}^n \varepsilon_{C_f,i}^2} \quad (9)$$

$$\max error = \max(|\varepsilon_{C_f,i}|), i = 1, \dots, n \quad (10)$$

The precision testing standards require that $RMSE \leq 0.05$, $\max error \leq 0.1$.

The optimization algorithm references [33,35,36] use the adaptive simulated annealing algorithm (ASA), which is an improved algorithm for the simulated annealing algorithm proposed by Ingber et al. It has better global solving ability and computational efficiency than the traditional SA algorithm and is an efficient and fast global optimization algorithm for solving difficult nonlinear optimization problems with multi-modal and non-smooth characteristics [30,31]. The convergence criterion for the optimization results in this study is $\varepsilon_{C_f} \leq 0.05$.

4. The Influence of the Design Parameters of the Ejector Nozzle on the Aerodynamic Performance

This chapter mainly introduces the contents of steps (1) and (2) in the optimization process and analyzes the results.

4.1. Case Design Based on Orthogonal Experimental Method

The variation range of design parameters was determined previously. Within the variation range, four levels were designed at equal intervals, resulting in a corresponding factor level table, as shown in Table 1.

Table 1. Factors and levels of ejector nozzle design parameters.

Level	Factor			
	A_s/A_p	A_e/A_p	L_s/D_p	L/D_p
1	1.23	1.44	0	1.10
2	1.44	1.93	0.15	1.28
3	1.64	2.42	0.3	1.47
4	1.85	2.91	0.45	1.65

For the four factors at four levels, an orthogonal array $L_{16}(4^5)$ [37] was employed to construct 16 initial sample points, as detailed in Table 2. Cases 11 and 16, with converging ejector nozzles, are excluded. Case 1 is utilized as the baseline ejector nozzle for reference.

Table 2. Computational cases of ejector nozzle based on orthogonal experiment design method.

Model	Factor				
	A_s/A_p	A_e/A_p	L_s/D_p	L/D_p	Blank
Case 1	1.23	1.44	0	1.10	1
Case 2	1.23	1.93	0.15	1.28	2
Case 3	1.23	2.42	0.3	1.47	3
Case 4	1.23	2.91	0.45	1.65	4
Case 5	1.44	1.93	0.3	1.10	4
Case 6	1.44	1.44	0.45	1.28	3
Case 7	1.44	2.91	0	1.47	2
Case 8	1.44	2.42	0.15	1.65	1
Case 9	1.64	2.42	0.45	1.10	2
Case 10	1.64	2.91	0.3	1.28	1
Case 11	1.64	1.44	0.15	1.47	4
Case 12	1.64	1.93	0	1.65	3
Case 13	1.85	2.91	0.15	1.10	3
Case 14	1.85	2.42	0	1.28	4
Case 15	1.85	1.93	0.45	1.47	1
Case 16	1.23	1.44	0	1.10	1

4.2. Flow Field Calculation Method

This article uses commercial software Fluent v 6.3 for numerical calculations, selecting a density-based two-dimensional N-S equation solver. The flow control equation is discretized using a second-order upwind scheme, and the turbulence model uses the SST k- ω model [38].

4.2.1. Flow Field Calculation Domain

The simulation calculations utilize a two-dimensional half-symmetric model. Figure 3 shows the flow field calculation domain. To mitigate potential influences on the results due to the computational domain, the calculation domain is $60R_{10}$ long and $10R_{10}$.

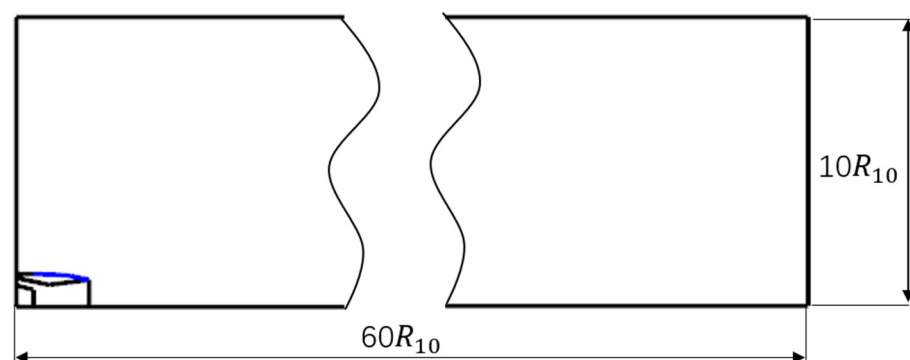


Figure 3. Flow field calculation domain diagram.

4.2.2. Boundary Conditions

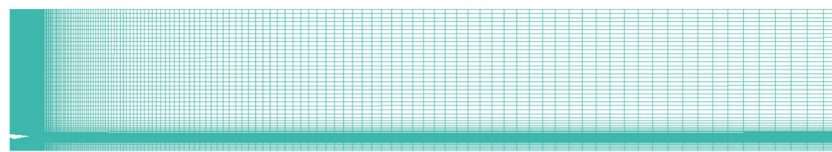
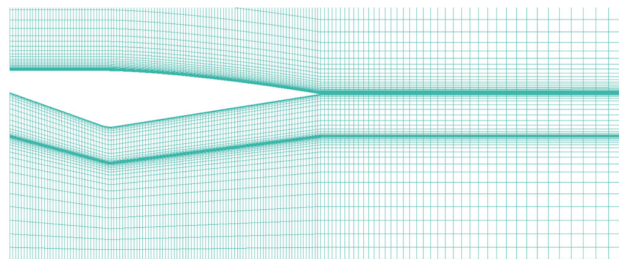
All walls are defined as no-slip walls. With the exception of the main nozzle wall, which is set as a coupled heat transfer boundary, all other wall surfaces are considered adiabatic. The main nozzle and ejector inlet are defined as pressure inlets, while the external flow field is configured as a pressure far-field. The specific values are shown in Table 3.

Table 3. Flow field boundary conditions of ejector nozzle.

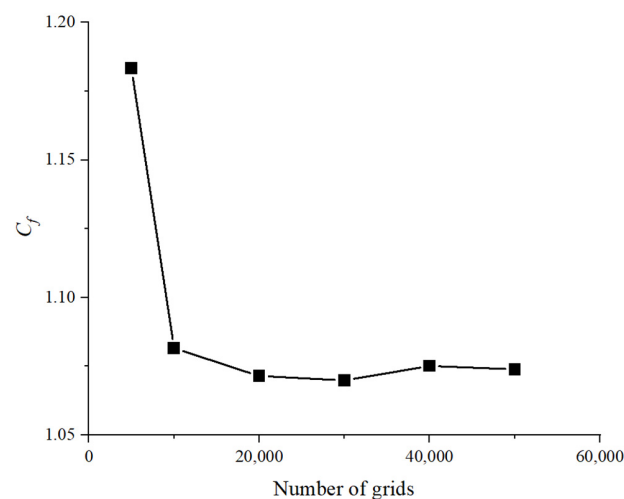
Boundary	Mach Number	Pressure	Temperature
Main nozzle inlet	—	$P_t/P_a = 4.83$	$T_t/T_a = 8.22$
Ejector inlet	—	$P_t/P_a = 1.90$	$T_t/T_a = 1.22$
External flow	1.05	P_a	T_a

4.2.3. Grid Division and Grid Independence Verification

Figure 4 shows the grid division of the entire calculation, and Figure 5 shows the results of local magnification of the nozzle region. As can be seen from the figure, the grid uses a structured grid to divide boundary layer mesh near the main nozzle wall, ejector sleeve wall, and aircraft rear body wall, while the downstream mesh of the nozzle is encrypted.

**Figure 4.** Grid diagram.**Figure 5.** Diagram of the grid near the wall.

To ensure computational accuracy while optimizing computational resources, a mesh independence study was conducted. Different grids were applied to the same ejector nozzle model, with the thrust coefficient used as a reference. The results for varying grid quantities are depicted in Figure 6. It is observed that after exceeding 20,000 grids, the variations become negligible. Therefore, considering computational efficiency and accuracy, the mesh quantity is maintained around 30,000.

**Figure 6.** Thrust coefficient comparison for grid independence verification.

4.3. Analysis of a Typical Ejector Nozzle Flow Field

Figure 7 presents the velocity vector field for Case 1. At different axial positions, red arrow sizes indicate velocity magnitude, while directions represent velocity vectors. It can be observed that the secondary flow initially has a slower velocity, creating a significant velocity gradient downstream of the main nozzle outlet in conjunction with the primary flow. The velocity continuously accelerates and becomes relatively constant near the outlet position.

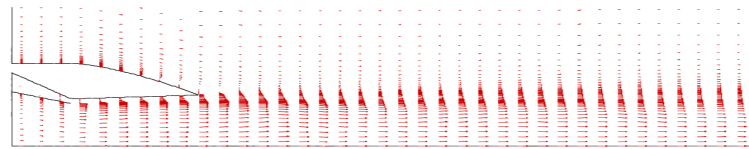


Figure 7. Velocity vector diagram of Case 1.

Figure 8 illustrates the streamlines for Case 1. The red, blue, and black streamlines originate from the main nozzle inlet, ejector inlet, and the external flow, respectively. From the streamlines, it is evident that both the primary and secondary flows continue to move outward near the nozzle outlet. Additionally, separation of the external flow occurs in the converging section, leading to eventual recirculation near the outlet.

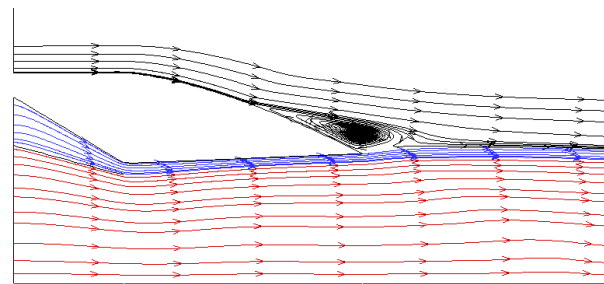


Figure 8. Streamlines diagram of Case 1.

Figure 9 depicts the Mach number contour plot for Case 1. It is evident that the Mach number reaches 1 at the main nozzle outlet for the primary flow, and it continues to expand and accelerate within the ejector nozzle. The external flow notably accelerates as it transitions from the straight to the converging section of the afterbody, leading to a significant decrease in Mach number at the location where recirculation occurs.

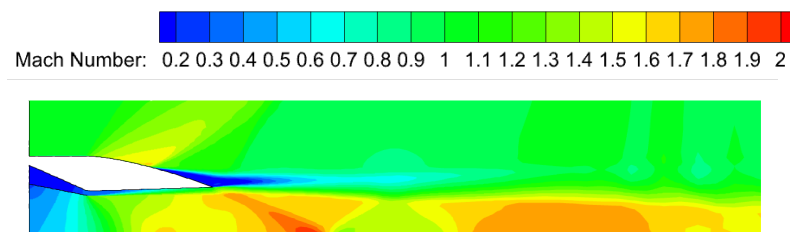


Figure 9. Mach number contour plot of Case 1.

Figure 10 provides the dimensionless pressure contour plot for Case 1, where P/P_a represents the ratio of local static pressure to ambient atmospheric pressure. It is observed that the jet at the ejector nozzle outlet is in an over-expanded state, leading to the appearance of shock structures downstream with a significant pressure increase. The accelerated external flow creates a pronounced low-pressure zone in the corresponding region.

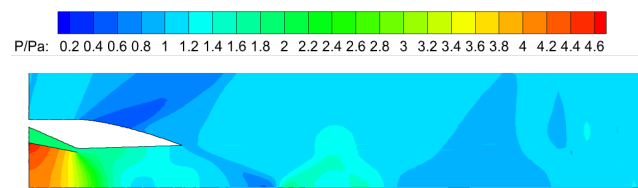


Figure 10. Dimensionless pressure contour plot of Case 1.

Figure 11 provides the dimensionless temperature contour plot for Case 1, where T/T_a represents the ratio of local static temperature to ambient atmospheric pressure. It can be seen from the figure that the primary flows out of the main nozzle outlet and expands directly to the wall of the ejector nozzle. The secondary flow all mixes with the primary flow, and the temperature near the wall of the ejector nozzle is slightly lower.

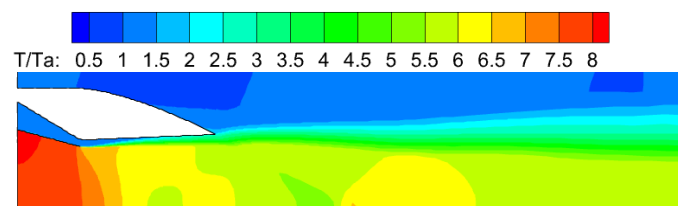


Figure 11. Dimensionless temperature contour plot of Case 1.

4.4. Direct Analysis of Aerodynamic Performance

Table 4 presents the aerodynamic performance results obtained from computational simulations based on the orthogonal experimental design.

Table 4. Aerodynamic performance of cases based on orthogonal experiment design method.

Model	\dot{m}_s/\dot{m}_p	C_f	C_{f-net}
Case 1	0.14139	1.00827	0.69932
Case 2	0.18958	1.05969	0.82563
Case 3	0.16241	0.94731	0.75585
Case 4	0.13001	0.86432	0.72661
Case 5	0.32305	1.04829	0.81417
Case 6	0.21405	1.02569	0.69514
Case 7	0.46181	1.01465	0.8803
Case 8	0.37017	1.03436	0.83509
Case 9	0.51736	1.06655	0.88605
Case 10	0.52007	1.04064	0.91061
Case 11	—	—	—
Case 12	0.46314	1.09612	0.82296
Case 13	0.85085	1.12905	1.00359
Case 14	0.75949	1.16576	0.97649
Case 15	0.60218	1.12707	0.85508
Case 16	—	—	—

The summarized results are organized in Table 5, where K_i represents the sum of corresponding aerodynamic performance values for each level i ($i = 1, 2, 3, 4$) of the geometric factors, and k_i denotes the arithmetic mean of the aerodynamic performance values obtained when the geometric factor is set to level i . R represents the range, defined as $R = \max \{k_1, k_2, k_3, k_4\} - \min \{k_1, k_2, k_3, k_4\}$. A larger range R for a geometric parameter indicates a more significant impact of the level variations of that parameter on the objective function.

Table 5. Direct analysis of influence of design parameters on aerodynamic performance.

		A_s/A_p	A_e/A_p	L_s/D_p	L/D_p	Blank
\dot{m}_s/\dot{m}_p	K1	0.62339	0.35545	1.82583	1.83265	1.63382
	K2	1.36908	1.57795	1.4106	1.68319	1.16875
	K3	1.50058	1.80942	1.00553	1.2264	1.69045
	K4	2.21252	1.96274	1.4636	0.96332	1.21254
	k1	0.15585	0.17772	0.45646	0.45816	0.40845
	k2	0.34227	0.39449	0.4702	0.4208	0.38958
	k3	0.50019	0.45236	0.33518	0.4088	0.42261
	k4	0.73751	0.49069	0.3659	0.32111	0.40418
	R	0.58166	0.31296	0.13502	0.13706	0.03303
	C_f	K1	3.87959	2.03396	4.28481	4.25218
K2		4.123	4.33118	3.22311	4.29178	3.14089
K3		3.20332	4.21399	3.03625	3.08903	4.19817
K4		3.42189	4.04867	4.08363	2.99481	3.07838
k1		0.9699	1.01698	1.0712	1.06304	1.05259
k2		1.03075	1.08279	1.07437	1.07295	1.04696
k3		1.06777	1.0535	1.01208	1.02968	1.04954
k4		1.14063	1.01217	1.02091	0.99827	1.02613
R		0.17073	0.07063	0.06229	0.07468	0.02646
C_{f-net}		K1	3.0074	1.39446	3.37908	3.40314
	K2	3.2247	3.31784	2.66431	3.40786	2.59198
	K3	2.61962	3.45348	2.48062	2.49123	3.27753
	K4	2.83516	3.52111	3.16288	2.38466	2.51727
	k1	0.75185	0.69723	0.84477	0.85078	0.82503
	k2	0.80618	0.82946	0.8881	0.85197	0.86399
	k3	0.87321	0.86337	0.82688	0.83041	0.81938
	k4	0.94505	0.88028	0.79072	0.79489	0.83909
	R	0.1932	0.18305	0.09738	0.05708	0.04461

Upon comparison, the influence of each design parameter on aerodynamic performance can be ranked as follows:

For \dot{m}_s/\dot{m}_p , the descending order of influence is A_s/A_p , A_e/A_p , L/D_p , L_s/D_p . For C_f , the descending order of influence is A_s/A_p , L/D_p , A_e/A_p , L_s/D_p . For C_{f-net} , the descending order of influence is A_s/A_p , A_e/A_p , L_s/D_p , L/D_p .

For all three aerodynamic parameters, A_s/A_p consistently emerges as the design parameter with the most significant impact.

The impact of design parameter variations on aerodynamic performance is illustrated in Figure 12, with each factor's level as the x-axis and the average values k_i of \dot{m}_s/\dot{m}_p , C_f , and C_{f-net} at each level as the y-axis. From the figure, it can be observed that with an increase in A_s/A_p , \dot{m}_s/\dot{m}_p , C_f , and C_{f-net} all exhibit a monotonically increasing trend. On the other hand, as A_e/A_p increases, \dot{m}_s/\dot{m}_p and C_{f-net} increase, while C_f first increases and then decreases.

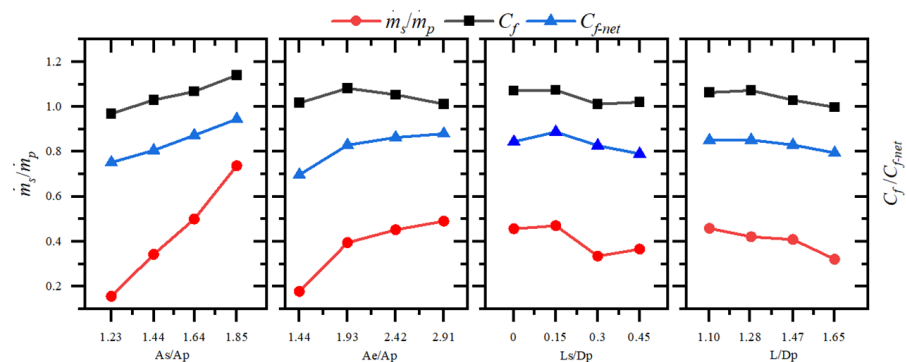


Figure 12. Influence of design parameters on aerodynamic performance of ejector nozzle.

5. Surrogate Model Accuracy Testing

The accuracy of the surrogate models was tested by calculating an additional 10 cases beyond the samples constructed in the orthogonal table. The results of the accuracy test are shown in Tables 6 and 7. The calculated values for the C_f surrogate model are $RMSE = 0.01010$ and $\max error = 0.02413$, while for the C_{f-net} surrogate model, $RMSE = 0.01743$ and $\max error = 0.04636$. The accuracy meets the requirements.

Table 6. Accuracy of surrogate model of C_f .

Model	A_s/A_p	A_e/A_p	L_s/D_p	L/D_p	$C_{f,CFD}$	$C_{f,Kriging}$	ε_{C_f}
Case 17	1.23	2.42	0.45	1.28	0.92789	0.9267	−0.00119
Case 18	1.23	2.91	0	1.47	0.9344	0.94945	0.01505
Case 19	1.23	1.44	0.3	1.65	0.99587	1.02	0.02413
Case 20	1.44	1.93	0	1.28	1.06628	1.0736	0.00732
Case 21	1.44	1.44	0.45	1.28	1.02558	1.0246	−0.00098
Case 22	1.64	2.42	0	1.28	1.1191	1.117	−0.0021
Case 23	1.64	2.42	0.45	1.47	1.07616	1.0649	−0.01126
Case 24	1.85	1.93	0.45	1.28	1.12789	1.1266	−0.00129
Case 25	1.85	2.42	0.15	1.10	1.15558	1.1608	0.00522
Case 26	1.85	2.91	0.15	1.65	1.13091	1.1291	−0.00181

Table 7. Accuracy of surrogate model of C_{f-net} .

Model	A_s/A_p	A_e/A_p	L_s/D_p	L/D_p	$C_{f-net,CFD}$	$C_{f-net,Kriging}$	$\varepsilon_{C_{f-net}}$
Case 17	1.23	2.42	0.45	1.28	0.7464	0.742549	−0.00385
Case 18	1.23	2.91	0	1.47	0.80009	0.800948	0.00086
Case 19	1.23	1.44	0.3	1.65	0.66082	0.707178	0.04636
Case 20	1.44	1.93	0	1.28	0.82328	0.817813	−0.00547
Case 21	1.44	1.44	0.45	1.28	0.69507	0.694903	−0.00017
Case 22	1.64	2.42	0	1.28	0.933	0.914527	−0.01847
Case 23	1.64	2.42	0.45	1.47	0.88308	0.885085	0.00201
Case 24	1.85	1.93	0.45	1.28	0.86593	0.854722	−0.01121
Case 25	1.85	2.42	0.15	1.10	0.97466	0.972219	−0.00244
Case 26	1.85	2.91	0.15	1.65	0.99306	1.002735	0.00967

6. Ejector Nozzle Profile Optimization Design

The design parameters and calculation results of the optimized model are shown in Table 8. Compared to the baseline model, the C_f of the max C_f ejector nozzle increased by 16.333%, and the C_{f-net} of the max C_{f-net} ejector nozzle increased by 46.674%.

Table 8. Comparison between baseline model and optimization models' aerodynamic performance.

Model	A_s/A_p	A_e/A_p	L_s/D_p	L/D_p	\dot{m}_s/\dot{m}_p	C_f	C_{f-net}
Case 1	1.23	1.44	0	1.102	0.1414	1.00827	0.69932
max C_f	1.85	2.4425	0	1.102	0.8489	1.17295	0.99296
max C_{f-net}	1.85	2.91	0	1.102	0.8690	1.15168	1.02572

Comparison of simulation results and predictions for the optimized profile are shown in Table 9, demonstrating that the optimization results meet the convergence criteria.

Table 9. Convergence criteria of two optimization models.

Max C_f			Max C_{f-net}		
$C_{f,CFD}$	$C_{f,Kriging}$	ε_{C_f}	$C_{f-net,CFD}$	$C_{f-net,Kriging}$	$\varepsilon_{C_{f-net}}$
1.17295	1.1664	−0.00558	1.02572	1.01856	−0.00698

Figure 13 presents a comparative illustration of the three models. Compared to the baseline model (Case 1), the two optimized models primarily exhibit an increase in A_s/A_p and A_e/A_p , while L/D_p and L_s/D_p remain unchanged. L/D_p has the maximum value within the variation range, and $L_s/D_p = 0$ indicates that the ejector nozzle throat is at the same section as the main nozzle outlet. In comparing the two optimized models, A_s/A_p is at its maximum value, A_e/A_p for the max C_f model is at the mid-range, and A_e/A_p for the max C_{f-net} model is at the maximum value within variation range.

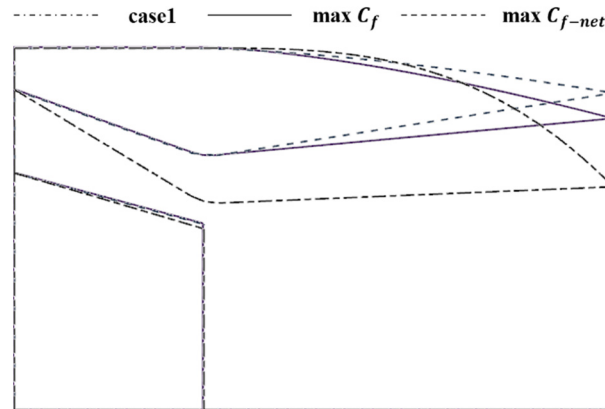


Figure 13. Comparison between baseline model and optimization models.

Figures 14–16 present the Mach number contour plot, dimensionless pressure contour plot, and dimensionless temperature contour plot for the two optimized models. From the figures, it can be observed that both optimized models are in a state of overexpansion. Due to the larger outlet area of the ejector nozzle in the max C_{f-net} model, it exhibits lower pressure near the outlet, resulting in a greater degree of overexpansion. The high-temperature area generated by shock waves at the outlet position is higher and the range is larger. However, this also effectively slows down the acceleration of the external flow in the converging section of the afterbody. In comparison with the pressure contour plot, the low-pressure region near the afterbody in the max C_{f-net} model is smaller. This explains why, despite having a lower C_f compared to the max C_f model, the max C_{f-net} model still has a higher C_{f-net} .

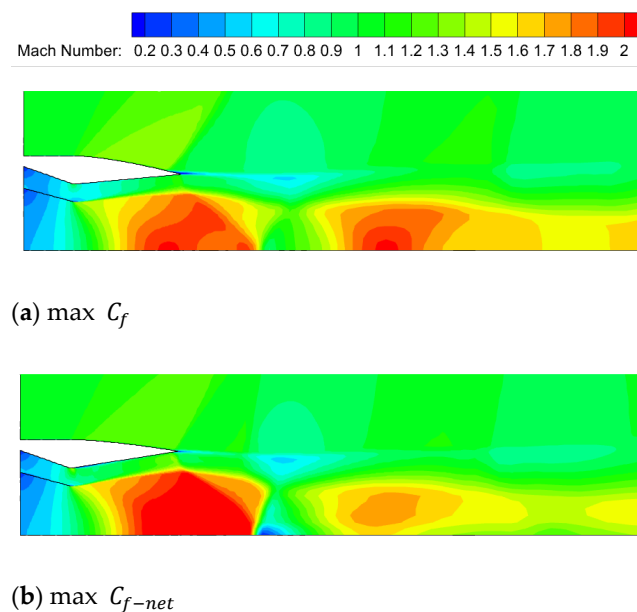
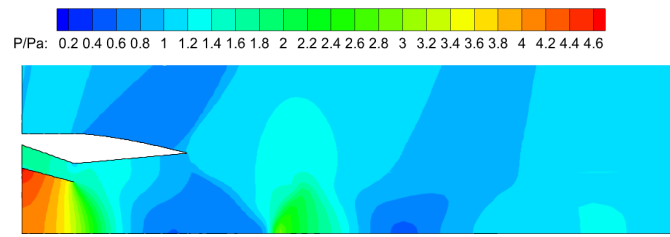
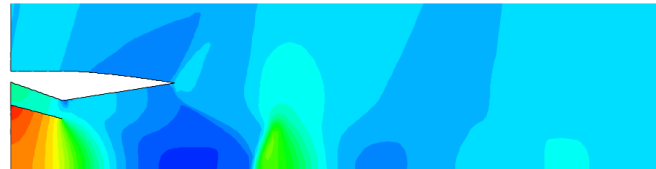


Figure 14. Mach number contour plot of optimization models.

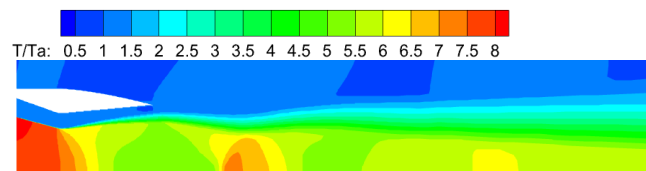


(a) max C_f

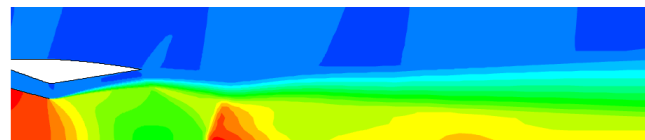


(b) max C_{f-net}

Figure 15. Dimensionless pressure contour plot of optimization models.



(a) max C_f



(b) max C_{f-net}

Figure 16. Dimensionless temperature contour plot of optimization models.

To more intuitively illustrate the impact of A_e/A_p variation on the afterbody drag, the pressure distribution on the afterbody surface for the two models is shown in Figure 17. It can be observed that in the max C_{f-net} model, the pressure on the afterbody surface decreases more gradually, and the lowest pressure point is closer to the ejector nozzle outlet.

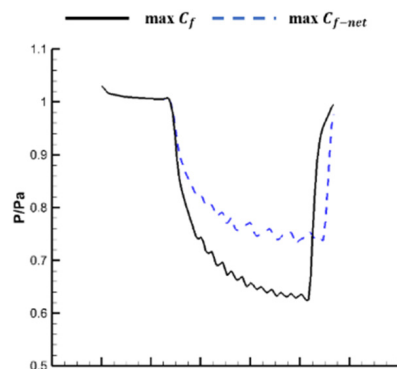


Figure 17. Comparison between two optimization models' afterbody wall dimensionless pressure.

7. Conclusions

In this paper, numerical simulation cases were designed using orthogonal experimental methods at a Mach number of 1.05, and the effects of the ejector nozzle throat area ratio A_s/A_p , outlet area ratio A_e/A_p , throat position L_s/D_p , and ejector nozzle length L/A_p on the ejector flow ratio, thrust coefficient, and net thrust coefficient of the ejector nozzle were investigated. Subsequently, optimization design was conducted with the goal of achieving the maximum thrust coefficient and net thrust coefficient. The following conclusions were drawn:

- (1) The factors that have the most significant influence on the aerodynamic performance of the ejector nozzle are A_s/A_p and A_e/A_p . An increase in A_s/A_p leads to an increase in \dot{m}_s/\dot{m}_p , C_f , and C_{f-net} of the ejector nozzle. On the other hand, an increase in A_e/A_p results in a decrease in \dot{m}_s/\dot{m}_p and C_f , but an increase in C_{f-net} .
- (2) The Kriging surrogate model combined with the adaptive simulated annealing (ASA) optimization algorithm demonstrates effective predictive capabilities for the aerodynamic performance of the ejector nozzle. In comparison with the baseline model, the max C_f model exhibits a 16.333% increase in C_f , while the max C_{f-net} model shows a substantial 46.674% enhancement in C_{f-net} .
- (3) For the ejector nozzle, being in an overexpanded state is advantageous for achieving greater thrust. Although increasing A_e/A_p may cause a loss in the thrust of the ejector nozzle, it effectively reduces the afterbody drag, thereby enhancing C_{f-net} .

Author Contributions: Conceptualization, H.J. and X.S.; methodology, H.J., X.S. and Y.H.; validation, X.S. and Y.H.; formal analysis, X.S.; investigation, Y.H.; data curation, Y.H.; writing—original draft preparation, H.J., X.S. and Y.H.; writing—review and editing, X.S. and Y.H. All authors have read and agreed to the published version of the manuscript.

Funding: This research was funded by the National Science and Technology Major Project (J2019-III-0009-0053).

Data Availability Statement: The data presented in this study are available on request from the corresponding author.

Conflicts of Interest: The authors declare no conflicts of interest.

Nomenclature

A	Area
R	Radius/Gas constant
D	Diameter/Drag
L	Axial length
F	Thrust
T	Static temperature
P	Pressure
U	Velocity
k	Specific heat ratio
\dot{m}	Mass flow rate
C_f	Thrust coefficient
p	Primary flow
s	Secondary flow
a	Air
e	Ejector nozzle
t	Total
Ma	Mach number

References

1. Starkey, R.; Lewis, M. Aerodynamics of a box constrained waverider missile using multiple scramjets. In Proceedings of the Joint Propulsion Conference & Exhibit, San Jose, CA, USA, 15–17 July 2013.
2. AIAA. Airframe/engine integration with variable cycle engines. In Proceedings of the 13th Propulsion Conference (AIAA), Huntsville, AL, USA, 17–19 July 2000.
3. Lewis, M.J. Application of waverider-based configurations to hypersonic vehicle design. In Proceedings of the 9th Applied Aerodynamics Conference, Baltimore, MD, USA, 23–25 September 1991; p. 3304.
4. O'Neill, M.K.L.; Lewis, M.J. Design tradeoffs on scramjet engine integrated hypersonic waverider vehicles. *J. Aircr.* **1993**, *30*, 943–952. [[CrossRef](#)]
5. Johnston, P.J.; Cabbage, J.M.; Weidner, J.P. Studies of Engine-Airframe Integration on Hypersonic Aircraft. *J. Aircr.* **1970**, *8*, 495–501. [[CrossRef](#)]
6. Carson, G.T.; Lee, E.E. *Experimental and Analytical Investigation of Axisymmetric Supersonic Cruise Nozzle Geometry at Mach Numbers from 0.60 to 1.30*; NASA: Washington, DC, USA, 1981.
7. Guan, T.; Zhang, J.Z.; Shan, Y. Effects of Tabbed-Nozzle on Pumping Performance of Incompressible Short Mixer-Ejector. *J. Propuls. Power* **2016**, *33*, 323–332. [[CrossRef](#)]
8. Li, H.; Wang, X.; Ning, J.; Zhang, P.; Huang, H.; Tu, J. Numerical Investigation of the nozzle expansion state and its effect on the performance of the steam ejector based on ideal gas model. *Appl. Therm. Eng.* **2021**, *199*, 117509. [[CrossRef](#)]
9. Wang, L.; Yan, J.; Wang, C.; Li, X. Numerical study on optimization of ejector primary nozzle geometries. *Int. J. Refrig.* **2017**, *76*, 219–229. [[CrossRef](#)]
10. Sun, W.; Ma, X.; Zhang, Y.; Jia, L.; Xue, H. Performance analysis and optimization of a steam ejector through streamlining of the primary nozzle. *Case Stud. Therm. Eng.* **2021**, *27*, 101356. [[CrossRef](#)]
11. Corda, S.; Moes, T.R.; Mizukami, M.; Hass, N.E.; Palumbo, N. *The SR-71 Test Bed Aircraft: A Facility for High-Speed Flight Research*; NASA: Washington, DC, USA, 2000.
12. Fang, C. *World Aeroengine Handbook*; Aviation Industry Press: Beijing, China, 1996.
13. Debonis, J.R. Full Navier-Stokes analysis of a two-dimensional mixer/ejector nozzle for noise suppression. In Proceedings of the 28th Joint Propulsion Conference and Exhibit, Monterey, CA, USA, 28–30 June 1992.
14. Addy, A.L.; Chow, W.L. Interaction between primary and secondary streams of supersonic ejector systems and their performance characteristics. *Aiaa J.* **1964**, *2*, 686–695.
15. Der, J. Improved methods of characterizing ejector pumping performance. *J. Propuls. Power* **1991**, *7*, 412–419. [[CrossRef](#)]
16. Stitt, L.E. *Exhaust Nozzles for Propulsion Systems with Emphasis on Supersonic Cruise Aircraft*; NASA: Washington, DC, USA, 1990.
17. Merati, P. Numerical Simulation of the Vortical Structures in a Lobed Jet Mixing Flow. In Proceedings of the 43rd AIAA Aerospace Sciences Meeting and Exhibit (AIAA), Reno, Nevada, 10–13 January 2005.
18. Liu, Y.H. Experimental and numerical research on high pumping performance mechanism of lobed exhaust-ejector mixer. *Int. Commun. Heat Mass Transf.* **2007**, *34*, 197–209. [[CrossRef](#)]
19. AIAA. Experimental investigation of three-dimensional forced mixer lobe flow fields. In Proceedings of the 1st National Fluid Dynamics Conference (AIAA), Cincinnati, OH, USA, 25–28 July 1988.
20. Axisymmetric, T.V.; Nozzles, E.; Lamb, M. *Internal Performance Characteristics of Thrust-Vectored Axisymmetric Ejector Nozzles*; National Aeronautics and Space Administration, Langley Research Center: Hampton, VA, USA, 1998.
21. Arun, K.R.; Rajesh, G. Physics of vacuum generation in zero-secondary flow ejectors. *Phys. Fluids* **2018**, *30*, 066102. [[CrossRef](#)]
22. Karthick, S.K.; Rao, S.M.V.; Jagadeesh, G.; Reddy, K.P.J. Parametric experimental studies on mixing characteristics within a low area ratio rectangular supersonic gaseous ejector. *Phys. Fluids* **2016**, *28*, 414. [[CrossRef](#)]
23. Hoter, Z.; Castner, R.S.; Zaman, K.Q. CFD Optimization of Ejector Flaps in a One-Sided Mixer Ejector Nozzle. In Proceedings of the AIAA Scitech 2019 Forum, San Diego, CA, USA, 7–11 January 2019.
24. Ge, C.; Xiao, L.; Shang, Y. Numerical Investigation of an Integrated Ejector Nozzle with the Nozzle Pressure Ratio of 2.97. *J. Phys. Conf. Ser.* **2021**, *1985*, 012022. [[CrossRef](#)]
25. Song, M.A.; Jianguo, T.; Zhiwei, Z.; Wei, Z.; Hao, J. Influence of secondary flow ejection on the performance of conformal asymmetric nozzle. *J. Natl. Univ. Def. Technol.* **2018**, *40*, 8.
26. Cai, J.; Li, Z.; Huang, H.; Zhang, K.; Tan, H. Numerical study on the flow characteristics of ejector nozzle with wide-speed range under cruise state. *J. Rocket. Propuls.* **2020**, *46*, 22–29.
27. Huang, H.; Zhang, K.; Tan, H.; Lu, S.; Zhao, L.; Lei, M.; Ling, W. Flow Characteristics of an Integrated Ejector Nozzle with Tertiary Intake. *J. Propuls. Technol.* **2020**, *41*, 2729–2738.
28. Li, Z.; Wang, H.; Huang, H. Analysis of Flow Field of Three-Dimensional Ejector Nozzle with Open-close Alternate Intake Valve at Transonic Velocity. *J. Aerosp. Power* **2023**, *38*, 2937–2947. [[CrossRef](#)]
29. Mattingly, J.D.; Heiser, W.H.; Daley, D.H. *Aircraft Engine Design*; American Institute of Aeronautics and Astronautics: Reston, VA, USA, 1987.
30. Lai, Y.; Jiang, X. *Detailed Explanation of Isight Parameter Optimization Theory and Examples*; Beijing University of Aeronautics and Astronautics Press: Beijing, China, 2012.
31. Wang, D.; Wang, J.; Wang, H.; Zhang, R.; Guo, Z. *Intelligent Optimization Method*; Higher Education Press: Beijing, China, 2007.

32. Wang, P.; Wang, Z.; Wu, Z.; Zhang, X.; Zhang, W. Optimization design for contour of pintle nozzle for variable thrust solid rocket motor under multiple working conditions. *J. Solid Rocket. Technol.* **2022**, *45*, 337–342.
33. Shi, X.; Ji, H. Numerical Investigation of Influence of Two-Dimensional Convergent and Divergent Nozzle's Design Parameters on Infrared Characteristics. *J. Aerosp. Power* **2020**, *35*, 944–955.
34. Wei, R.; Du, G.; Jin, J. Optimization of trailing edge angles of single expansion ramp nozzle based on Kriging Method. *J. Aerosp. Power* **2018**, *33*, 874–881. [[CrossRef](#)]
35. Shi, X.; Ji, H. Optimization design of two dimensional convergent and divergent nozzles' profile based on surrogate models. *J. Aerosp. Power* **2016**, *8*, 2124–2131.
36. Shi, X.; Feng, W.; Ji, H. Multi-objective Contour Optimization Design of Thrust and Infrared Characteristics of Two-Dimensional Exhaust System of Turbofan Engine. *J. Nanjing Univ. Aeronaut. Astronaut.* **2023**, *55*, 597–605. [[CrossRef](#)]
37. Qiu, Y. *Experimental Design and Data Processing*; University of Science and Technology of China Press: Hefei, China, 2008.
38. Bartosiewicz, Y.; Aidoun, Z.; Desevaux, P.; Mercadier, Y. Numerical and experimental investigations on supersonic ejectors. *Int. J. Heat Fluid Flow* **2005**, *26*, 56–70. [[CrossRef](#)]

Disclaimer/Publisher's Note: The statements, opinions and data contained in all publications are solely those of the individual author(s) and contributor(s) and not of MDPI and/or the editor(s). MDPI and/or the editor(s) disclaim responsibility for any injury to people or property resulting from any ideas, methods, instructions or products referred to in the content.